Chapter 6

Calculating Free Modes of Oscillation in Complex Geometries

In this chapter, the calculation of free modes of oscillation in the linear rotating shallow water framework is considered. The DG-FEM method used in Chapters 4 and 5 is employed so that its geometric flexibility can be exploited to explore closed basins of arbitrary shape. In the following sections, the numerical methodology is introduced and explained. The method is then validated against analytical solutions and applied to basins with both simple and irregular geometries.

6.1 History and motivation

The calculation of free modes of oscillation in closed rotating basins represents a thoroughly-studied problem with previous works dating back well over a century [71, 119]. The importance of free modes of oscillation in understanding basin-scale dynamics in large lakes is thus well-known, and a method that can calculate these modes on numerical grids that accurately reflect the actual geometry of real-world lakes is very desirable since these numerically calculated modes allow hypotheses regarding the basin-scale dynamics of lakes to be formulated and tested against field data.

Analytical formulae for the free modes of oscillations in infinite non-rotating and rotating channels were among the first successfully calculated. It was also attempted to use so-called one-dimensional channel theory to estimate the longitudinal oscillations of Lake Erie [96] and the other great lakes [103]. Analytical expressions were also calculated for idealized rotating circular [71, 25, 115] and elliptical basins [3]. Calculations of the internal free modes of oscillation have also been explored in idealized basins by means of a normal modes decomposition in [25, 3].

Numerical calculations were then performed by [98, 100] using finite difference methods. The method of Rao and Schwab [100] uses an analytical reduction by using a series decomposition in terms of divergence-free and irrotational basis functions. The main difficulty with the method of Rao and Schwab lay with ensuring the eigenspectrum of basis functions is orthogonal. While their method is able to compute modes in general (arbitrarily-shaped) basins, the method can only represent the coastline in a piece-wise constant manner. Hamblin [57] computed the free modes of oscillation by re-casting the equations as a variational optimization problem that was solved using the finite element method, allowing for more flexibility in accurately representing coastlines in a piece-wise linear and curvilinear manner. Due to the limited availability of computing power in the 1970–1980 time-frame, it is perhaps not surprising that these calculations were done with very coarse grids by today's standards, and the problem is worthy of being revisited with modern computers and discretization methods.

In this work, we employ the analytical reduction methodology of [100] in closed basins represented by triangular grids using the symmetric interior penalty discontinuous Galerkin finite element method (hereafter, SIP-DG). The key ideas of the methodology thus remains the same as in [100], and only the numerical details differ. The method represents an improvement over the method of [100] since it allows the coastline to be represented in a piece-wise linear manner. Furthermore, the SIP-DG method allows more accurate solutions to be obtained quite simply by increasing the order of the local basis polynomials used on each triangle without affecting the size of the computational stencil. The methodology of [100] also requires special care in constructing the numerical grid, since a staggered grid is required to ensure the spatial discretization operators are symmetric to guarantee the orthogonality of the basis of eigenfunctions. With the SIP-DG method, the spatial discretization operator is, by construction, guaranteed to be symmetric regardless of where the grid points are collocated. This additional flexibility requires little work to be done by the individual performing the calculation of the modes aside from generating the triangular mesh.

An alternative to the SIP-DG method that one may consider to obtain solutions on unstructured triangular meshes is the Continuous Galerkin (CG) finite element method (FEM) or its high-order extension, the spectral element method (SEM) [68]. However, it is known that the CG-based methods can result in spurious (numerical) modes that can pollute the physical part of the eigenspectrum [60]. In some cases, such spurious modes can be convergent [60] as one refines the computational grid and may lead to the rather undesirable result where they are mistaken for physical modes. Additionally, FEM discretizations may also contain so-called "pesky modes" that converge to being members of the operator null space as the grid is refined [24]), leading to difficulties for iterative solvers. The SIP-DG method circumvents this issue by suppressing any spurious modes to unphysically high frequencies, ensuring that they will not be present in any reasonable truncation of the eigenspectrum. This suppression of spurious modes is furnished by the use of a penalty parameter, that guarantees that the spurious modes do not pollute the physical part of the spectrum provided that it is taken to be sufficiently large.

In the following, we present our numerical methodology for calculating the free modes of oscillation in rotating basins of arbitrary geometry followed by validation cases, a case study of an idealized basin, and applications to real-world lakes.

6.2 Methods

The linearized shallow water equations on the rotating f-plane can be written as

$$\frac{\partial \mathbf{M}}{\partial t} + f\mathbf{M}^{\perp} = -gH\nabla\eta \tag{6.1}$$

$$\frac{\partial \eta}{\partial t} + \nabla \cdot \mathbf{M} = 0 \tag{6.2}$$

where $H(\mathbf{x})$ is allowed to vary in space in terms of the Cartesian position vector $\mathbf{x} = (x, y)$, $\eta(\mathbf{x}, t)$ is the free surface elevation above the undisturbed state, $\mathbf{M} = H\mathbf{u}$ is the volume transport vector, $\mathbf{u} = (u(\mathbf{x}, t), v(\mathbf{x}, t))$ is the fluid velocity field, and superscript $\perp$ denotes rotation by 90° counter-clockwise, so that $\mathbf{M}^{\perp} = H(-v, u)$. The parameters g and f represent the acceleration due to gravity and the Coriolis parameter, respectively. The fluid depth is non-dimensionalized via $H(\mathbf{x}) = \overline{H}h(\mathbf{x})$, where $\overline{H}$ is the mean basin depth and $h(\mathbf{x})$ is dimensionless.

As explained in [100], combining equations (6.1)–(6.2) to find an equation for η yields an operator that is not self-adjoint. Further difficulty results from the fact that the no normal flow boundary condition in terms of η contains real and imagninary components and is coupled to the eigenvalue (the frequency). To circumvent these difficulties, a Helmholtz decomposition is applied to the volume transport vector in order to express it in terms of a velocity potential and a streamfunction, i.e.,

$$\mathbf{M} = -h\nabla\phi + \nabla^{\perp}\psi \ , \tag{6.3}$$

where $\nabla^{\perp} = \left(-\frac{\partial}{\partial y}, \frac{\partial}{\partial x}\right)$, and ϕ and ψ satisfy the no normal flow boundary condition

$$\frac{\partial \phi}{\partial n} = \psi = 0 \quad \text{on} \quad \partial\Omega \,. \tag{6.4}$$

where $\frac{\partial \phi}{\partial n} = \nabla\phi \cdot \hat{\mathbf{n}}$ represents the derivative taken in the direction normal to $\partial\Omega$, the boundary of a closed basin (domain), Ω. The no-normal flow condition on ψ actually requires ψ to be constant along the boundary. However, since only the derivatives of ψ are of physical relevance, the constant is set to zero without loss of generality.

The decomposition (6.3) is unique. That is, assuming $\mathbf{M}$ is known, ϕ is the unique solution of

$$\begin{aligned} \nabla \cdot (h\nabla\phi) + \nabla \cdot \mathbf{M} &= 0 \,, \quad \text{on} \quad \Omega \,, \\ \frac{\partial \phi}{\partial n} &= 0 \,, \quad \text{on} \quad \partial\Omega \,, \end{aligned} \tag{6.5}$$

as can be seen by taking the divergence of (6.3). Similarly, ψ is the unique solution of

$$\begin{aligned} \nabla \times \left(\frac{1}{h}\nabla^{\perp}\psi\right) - \nabla \times \left(\frac{1}{h}\mathbf{M}\right) &= 0 \,, \quad \text{on} \quad \Omega \,, \\ \psi &= 0 \,, \quad \text{on} \quad \partial\Omega \,. \end{aligned} \tag{6.6}$$

The next step is to form two sets of basis functions based on two eigenvalue problems. We define the set $\{\phi_\alpha, \lambda_\alpha\}_{\alpha=1}^{N_\phi}$ given by the eigenproblem

$$\nabla \cdot (h\nabla\phi_\alpha) + \lambda_\alpha\phi_\alpha = 0 \,, \quad \text{on} \quad \Omega \,, \tag{6.7}$$

$$\nabla\phi_\alpha \cdot \hat{\mathbf{n}} = 0 \,, \quad \text{on} \quad \partial\Omega \,, \tag{6.8}$$

and the set $\{\psi_\alpha, \mu_\alpha\}_{\alpha=1}^{N_\psi}$ given by

$$\nabla \cdot \left(\frac{1}{h}\nabla\psi_\alpha\right) + \mu_\alpha\psi_\alpha = 0 \,, \quad \text{on} \quad \Omega \,, \tag{6.9}$$

$$\psi_\alpha = 0 \,, \quad \text{on} \quad \partial\Omega \,. \tag{6.10}$$

Here, N_ϕ and N_ψ are taken as finite integers to truncate the bases for computational reasons. It can be shown using dimensional analysis that a suitable normalization for the basis functions is

$$\iint\limits_{\Omega} h\nabla\phi_k \cdot \nabla\phi_l dA = \lambda_l \iint\limits_{\Omega} \phi_k\phi_l dA = Ac^2\overline{H}^2\delta_{k,l} \,, \tag{6.11}$$

$$\iint\limits_{\Omega} \frac{1}{h}\nabla^{\perp}\psi_k \cdot \nabla^{\perp}\psi_l dA = \mu_l \iint\limits_{\Omega} \psi_k\psi_l dA = Ac^2\overline{H}^2\delta_{k,l} \,. \tag{6.12}$$

Next, ϕ and ψ are expanded in terms of the basis functions via

$$\phi = \sum_\alpha P_\alpha(t)\phi_\alpha \ , \tag{6.13}$$

$$\psi = \sum_\alpha Q_\alpha(t)\psi_\alpha \ . \tag{6.14}$$

Now, since

$$\eta_t = -\nabla \cdot \mathbf{M} = \nabla \cdot (h\nabla\phi) = -\sum_\alpha P_\alpha \lambda_\alpha \phi_\alpha \ , \tag{6.15}$$

it is clear that η should be expanded in terms of the ϕ_α's. Rao and Schwab [100] set

$$\eta = \sum_\alpha R_\alpha(t)\eta_\alpha = \sum_\alpha R_\alpha(t)\frac{\lambda_\alpha^{\frac{1}{2}}}{c}\phi_\alpha \ , \tag{6.16}$$

such that the R_α's are dimensionless, just as the P_α's and Q_α's are, by construction.

For the momentum equation (6.1), we can use

$$\mathbf{M} = -h\nabla\phi + \nabla^\perp\psi \ , \tag{6.17}$$

$$= -h\sum_\alpha P_\alpha(t)\nabla\phi_\alpha + \sum Q_\alpha(t)\nabla^\perp\psi_\alpha \ , \tag{6.18}$$

and

$$\mathbf{M}^\perp = (-h\nabla\phi + \nabla^\perp\psi)^\perp = -h\nabla^\perp\phi - \nabla\psi \ , \tag{6.19}$$

to find

$$\begin{aligned} -\sum_\alpha \frac{dP_\alpha}{dt}h\nabla\phi_\alpha + \sum_\alpha \frac{dQ_\alpha}{dt}\nabla^\perp\psi_\alpha \quad &- \quad fh\sum_\alpha P_\alpha \nabla^\perp\phi_\alpha - f\sum_\alpha Q_\alpha\nabla\psi_\alpha \\ &= \quad -g\overline{H}h\sum_\alpha R_\alpha \frac{\lambda_\alpha^{\frac{1}{2}}}{c}\nabla\phi_\alpha \ . \end{aligned} \tag{6.20}$$

Equation (6.20) can be simplified by taking the dot product with $\nabla\phi_\beta$, using the normalization (6.11), and the orthogonality relation

$$\iint_\Omega \nabla^\perp\psi_\alpha \cdot \nabla\phi_\beta \, dA = 0 \ , \tag{6.21}$$

that can be established using integration by parts. This simplification yields

$$\begin{aligned}\frac{dP_\beta}{dt} &+ \sum_\alpha P_\alpha \left(\frac{1}{Ac^2\overline{H}^2} \iint\limits_\Omega fh\nabla\phi_\beta \cdot \nabla\phi_\alpha^\perp \, dA \right) \\ &+ \sum_\alpha Q_\alpha \left(\frac{1}{Ac^2\overline{H}^2} \iint\limits_\Omega f\nabla\psi_\alpha \cdot \nabla\phi_\beta \, dA \right) = c\lambda_\beta^{\frac{1}{2}} R_\beta \ ,\end{aligned} \tag{6.22}$$

which may be written in terms of matrices as

$$\frac{dP_\beta}{dt} - \sum_\alpha A_{\beta\alpha} P_\alpha - \sum_\alpha B_{\beta\alpha} Q\alpha - \nu_\beta R_\beta = 0 \ , \text{(no sum over } \beta) \ , \tag{6.23}$$

where

$$A_{\beta\alpha} = -\frac{1}{Ac^2\overline{H}^2} \iint\limits_\Omega fh\nabla\phi_\beta \cdot \nabla^\perp\phi_\alpha \, dA \ , \tag{6.24}$$

$$B_{\beta\alpha} = -\frac{1}{Ac^2\overline{H}^2} \iint\limits_\Omega f\nabla\psi_\alpha \cdot \nabla\phi_\beta \, dA \ , \tag{6.25}$$

$$\nu_\beta = c\lambda_\beta^{\frac{1}{2}} \ . \tag{6.26}$$

Similarly, $\frac{dP_\alpha}{dt}$ can be eliminated from (6.20) by taking its dot product with $\frac{1}{h}\nabla^\perp\psi_\beta$ along with the normalization (6.12) and the orthogonality relation

$$\iint\limits_\Omega \nabla^\perp\psi_\beta \cdot \nabla\phi_\alpha \, dA = 0 \ . \tag{6.27}$$

Doing so gives

$$Ac^2\overline{H}^2 \frac{dQ_\beta}{dt} - \sum_\alpha P_\alpha \iint\limits_\Omega \nabla^\perp\phi_\alpha \cdot \nabla^\perp\psi_\beta \, dA - \sum_\alpha Q_\alpha \iint\limits_\Omega f\nabla\psi_\alpha \cdot \frac{1}{h}\nabla^\perp\psi_\beta \, dA = 0 \ , \tag{6.28}$$

or in matrix form

$$\frac{dQ_\beta}{dt} - \sum_\alpha C_{\beta\alpha} P_\alpha - \sum_\alpha D_{\beta\alpha} Q_\alpha = 0 \ . \tag{6.29}$$

where

$$\begin{aligned} C_{\beta\alpha} &= \frac{1}{Ac^2\overline{H}^2}\iint\limits_{\Omega} f\nabla^{\perp}\phi_\alpha\cdot\nabla^{\perp}\psi_\beta\, dA\ , \\ &= \frac{1}{Ac^2\overline{H}^2}\iint\limits_{\Omega} f\nabla\phi_\alpha\cdot\nabla\psi_\beta\, dA\ , \\ &= -B_{\alpha\beta}\ , \end{aligned} \tag{6.30}$$

and

$$D_{\beta\alpha} = \frac{1}{Ac^2\overline{H}^2}\iint\limits_{\Omega} f\frac{1}{h}\nabla\psi_\alpha\cdot\nabla^{\perp}\psi_\beta\ . \tag{6.31}$$

The fact that C and B share this symmetry property will have important consequences momentarily, along with the fact that A and D are anti-symmetric, i.e.,

$$A_{\beta\alpha} = -A_{\alpha\beta}\ , \tag{6.32}$$

$$D_{\beta\alpha} = -D_{\alpha\beta}\ , \tag{6.33}$$

which can be demonstrated by first noticing that $\nabla\phi_\beta\cdot\nabla^{\perp}\phi_\alpha = \nabla\phi_\alpha\cdot\left(-\nabla^{\perp}\phi_\beta\right)$. The system of ordinary differential equations for $(P_\alpha, Q_\alpha, R_\alpha)$ must be closed by substituting the expansion (6.16) into equation (6.2), resulting in

$$\sum_\alpha \frac{dR_\alpha}{dt}\frac{\lambda_\alpha^{\frac{1}{2}}}{c}\phi_\alpha + \sum_\alpha P_\alpha\nabla\cdot(-h\nabla\phi_\alpha) = 0\ . \tag{6.34}$$

This equation can be simplified by multiplying by ϕ_β, integrating over the domain, and exploiting orthogonality, via

$$\sum_\alpha \frac{dR_\alpha}{dt}\frac{\lambda_\beta^{\frac{1}{2}}}{c}\frac{Ac^2\overline{H}^2}{\lambda_\beta}\delta_{\alpha\beta} - \sum_\alpha P_\alpha\iint\limits_{\Omega}\phi_\beta\nabla\cdot(h\nabla\phi_\alpha)\ dA = 0\ . \tag{6.35}$$

After simplifying, we find

$$\frac{dR_\beta}{dt} + \nu_\beta P_\beta = 0\ , \quad \text{(no sum)}\ . \tag{6.36}$$

Equations (6.23), (6.29), and (6.36) may be combined into the standard form of a system of ODEs

$$\frac{d}{dt}\mathbf{V} + E\mathbf{V} = 0\ , \tag{6.37}$$

where

$$\mathbf{V} = \begin{pmatrix} P \\ Q \\ R \end{pmatrix} , \quad \text{and} \quad E = \begin{pmatrix} -A & -B & -<\nu> \\ -C & -D & 0 \\ <\nu> & 0 & 0 \end{pmatrix} , \tag{6.38}$$

and

$$<\nu>= \begin{pmatrix} \nu_1 & 0 & \dots & 0 \\ 0 & \nu_2 & \dots & 0 \\ \vdots & \vdots & \ddots & \vdots \\ 0 & 0 & \dots & \nu_{N_\phi} \end{pmatrix} = \operatorname{diag}(\nu_i) \ . \tag{6.39}$$

The eigenvalue problem for the horizontal modes of the system can be recovered by looking for time-periodic solutions, i.e., by assuming

$$\mathbf{V}(t) = \mathrm{e}^{i\sigma t}\hat{\mathbf{V}} \ , \tag{6.40}$$

where

$$\hat{\mathbf{V}} = \begin{pmatrix} \hat{P} \\ \hat{Q} \\ \hat{R} \end{pmatrix} \tag{6.41}$$

is constant in time. The substitution of this ansatz yields the eigenvalue problem

$$iE\hat{\mathbf{V}} = \sigma\hat{\mathbf{V}} \ . \tag{6.42}$$

Inspecting the structure of E and recalling that the matrices A and D are symmetric, $B = -C^{\mathsf{T}}$, it follows that E is anti-symmetric. Therefore, iE is Hermitian and the eigenvalues σ are real. Furthermore, since iE is purely imaginary and σ is purely real, it follows that all eigenvectors must have real and imaginary components in order to satisfy the eigenproblem (6.42). Physically, this property corresponds to the various basis functions being out of phase with one another.

6.2.1 Obtaining basis functions from the Symmetric Interior Penalty Discontinuous Galerkin (SIP-DG) method

The above section deals with the theory behind the analytical reduction methodology used to compute the modes. It assumes that two orthogonal sets of basis functions resulting from homogenous eigenvalue problems are known *a priori*. In basins of general shape, the basis functions must be constructed numerically, and we achieve this through the symmetric interior penalty disconuous Galerkin (SIP-DG) as we explain below.

Consider, without loss of generality, the eigenvalue problem for the unknown eigenpair (μ, ϕ),

$$\nabla \cdot (h \nabla \phi) = \mu \phi \ . \tag{6.43}$$

As explained by [60], in order to discretize an elliptic operator with the DG method it is necessary to re-write the problem as a first-order system of equations by introducing the auxiliary variable

$$\mathbf{q} = (q_x, q_y) = \sqrt{h} \nabla \phi \ . \tag{6.44}$$

After having done so, the first-order system reads

$$\nabla \cdot \left(\sqrt{h} \mathbf{q} \right) = \mu \phi \ , \tag{6.45}$$

$$q_x = \sqrt{h} \frac{\partial \phi}{\partial x} \ , \tag{6.46}$$

$$q_y = \sqrt{h} \frac{\partial \phi}{\partial y} \ . \tag{6.47}$$

It is then assumed the domain Ω is partitioned into K triangular sub-domains (elements). We apply the nodal DG methodology, and assume that each of the unknown approximate solution fields can be represented locally on a particular triangle $\mathbf{D}^k$ in terms of two-dimensional Lagrange interpolating polynomials, i.e.,

$$\phi^k(\mathbf{x}) = \sum_{i=1}^{N_p} \phi^k(\mathbf{x}_i^k) \ell_i^k(\mathbf{x}) \ , \tag{6.48}$$

and similar definitions exist for q_x^k and q_y^k. Here $\{\mathbf{x}_i^k\}_{i=1}^{N_p}$ is the set of N_p nodes used to represent the solution on a triangle $\mathbf{D}^k$ with N_p dependent on the order of approximation. The weak form of equation (6.45) is obtained by substituting the approximate local solution functions, multiplying by a member of the space of local test functions $V^k = \{\ell_j^k\}_{j=1}^{N_p}$ and integrating by parts, yielding

$$\int_{\partial \mathbf{D}^k} \ell_j^k (\sqrt{h}\mathbf{q})^* \cdot \hat{\mathbf{n}}^k \, d\mathbf{x} - \int_{\mathbf{D}^k} \left(\sqrt{h}^k \mathbf{q}^k \right) \cdot \nabla \ell_j^k \, d\mathbf{x} = \mu \int_{\mathbf{D}^k} \ell_j^k \phi^k \, d\mathbf{x} \ , \tag{6.49}$$

where $(\sqrt{h}\mathbf{q})^*$ is a numerical flux function used to weakly impose continuity across element interfaces and $\hat{\mathbf{n}} = (n_x, n_y)$ is the unit outward normal to an element edge. For computational convenience, we calculate the strong form of equations (6.46)–(6.47) where integration by parts is performed twice instead of once. This gives

$$\int_{\mathbf{D}^k} \ell_j^k q_x^k d\mathbf{x} = \int_{\mathbf{D}^k} \ell_j^k \sqrt{h}^k \frac{\partial \phi^k}{\partial x}\, d\mathbf{x} - \int_{\partial \mathbf{D}^k} \ell_j^k \left((\sqrt{h}\phi)^k - (\sqrt{h}\phi)^* \right) n_x^k \, d\mathbf{x} \,, \tag{6.50}$$

$$\int_{\mathbf{D}^k} \ell_j^k q_y^k d\mathbf{x} = \int_{\mathbf{D}^k} \ell_j^k \sqrt{h}^k \frac{\partial \phi^k}{\partial y}\, d\mathbf{x} - \int_{\partial \mathbf{D}^k} \ell_j^k \left((\sqrt{h}\phi)^k - (\sqrt{h}\phi)^* \right) n_y^k \, d\mathbf{x} \,. \tag{6.51}$$

In the symmetric interior penalty (SIP-DG) method, the numerical fluxes are taken to be

$$(\sqrt{h}\mathbf{q})^* = \{\!\{\sqrt{h}\nabla\phi\}\!\} - \tau[\![\sqrt{h}\phi]\!] \,, \tag{6.52}$$

$$(\sqrt{h}\phi)^* = \{\!\{\sqrt{h}\phi\}\!\} \,. \tag{6.53}$$

Here,

$$\{\!\{\mathbf{u}\}\!\} = \frac{\mathbf{u}^- + \mathbf{u}^+}{2}, \qquad [\![\mathbf{u}]\!] = \hat{\mathbf{n}}^- \cdot \mathbf{u}^- + \hat{\mathbf{n}}^+ \cdot \mathbf{u}^+ \,, \tag{6.54}$$

represent the average and jump in some quantity, $\mathbf{u}$, across the interface, with superscripts $-$ and $+$ referring to information interior to and exterior to the element, respectively.

Following the discussion in Section 4.6, the integral formulations are written in terms of local matrix operators and the auxiliary variable $\mathbf{q}$ is elminated locally so that a global stiffness matrix operator can be set up directly in sparse matrix format. Similarly, a global mass matrix operator may be constructed trivially since it is block diagonal with each block given by $\mathcal{M}^k$. In terms of global matrix operators, we see that the discretized Poisson eigenvalue problem takes the form of a generalized matrix eigenvalue problem,

$$K\boldsymbol{\phi} = \mu M \boldsymbol{\phi} \,, \tag{6.55}$$

where K is the global stiffness matrix and M is the global mass matrix. Both are guaranteed to be symmetric, and $\boldsymbol{\phi} = \bigoplus_{k=1}^{K} \boldsymbol{\phi}^k$ is the global solution vector.

6.2.2 Constructing the Modes

Computing the eigenvalues of the eigenvalue problem (6.42) yields the frequencies σ and eigenvectors for $2N_\phi$ gravitational modes and N_ψ rotational modes. Rotational modes exist purely due to changes in potential vorticity in the background state that, under quasi-geostrophic theory [70], can only occur due to changes in the lake's depth H or variations in the Coriolis parameter f. In this work, we ignore variations in f by invoking the f-plane approximation, and we only find rotational modes when bathymetric variations are included.

The computed frequencies (eigenvalues) come in pairs with one the negative of the other, and their corresponding eigenvectors are complex conjugates of one another. This is to be expected since one can show that if $(\sigma, \hat{\mathbf{V}})$ is an eigenpair of (6.42), then $(-\sigma, \overline{\hat{\mathbf{V}}})$ is also an eigenpair, where $\overline{}$ denotes complex conjugation. Physically, these two eigenpairs correspond to the same mode since

$$\Re\left(\hat{\eta}(x,y)\mathrm{e}^{i\sigma t}\right) = \Re\left(\overline{\hat{\eta}(x,y)\mathrm{e}^{i\sigma t}}\right) = \Re\left(\overline{\hat{\eta}(x,y)}\mathrm{e}^{i(-\sigma)t}\right) \ . \tag{6.56}$$

Hence, of the $2N_\phi + N_\psi$ computed modes, only half of them are physically distinct.

The spatial structure of each mode $(\hat{\eta}, \hat{\phi}, \hat{\psi})$ can be computed by summing the series (6.13)-(6.14) and (6.16) using the coefficients for $(\hat{P}, \hat{Q}, \hat{R})$ that are given by the entries of $\hat{\mathbf{V}}$. Since the computed modes contain both real and imaginary parts, it is useful to write the free surface in terms of an amplitude $A(x,y)$ and a phase angle $\theta(x,y)$ as follows:

$$\begin{aligned} \eta(x,y,t) &= \Re\left(\hat{\eta}(x,y)\mathrm{e}^{i\sigma t}\right) \\ &= A(x,y)\cos(\sigma t - \theta(x,y)) \ , \end{aligned} \tag{6.57}$$

where

$$\hat{\eta}(x,y) = \hat{\eta}_r(x,y) + i\hat{\eta}_i(x,y) \ , \tag{6.58}$$

$$A(x,y) = \sqrt{\hat{\eta}_r^2 + \hat{\eta}_i^2} \ , \tag{6.59}$$

$$\theta(x,y) = \tan^{-1}\left(-\frac{\hat{\eta}_i}{\hat{\eta}_r}\right) \ . \tag{6.60}$$

In the results below, we numerically compute $\theta(x,y)$ using the four-quadrant inverse tangent function to obtain angles between $-180°$ and $180°$. By construction, high water propagates in the direction of increasing θ, and hence θ gives insight into the direction of rotation and propagation properties of the modes.

6.3 Validation – internal Kelvin and Poincaré waves in a circular basin

As a means of validating our numerical method, we have reproduced the analytical calculations performed by [25] for a two-layer flat-bottomed circular basin of radius $r_0 = 67.5$ km representing a model of a large mid-latitude lake. The acceleration due to gravity and Coriolis parameter were taken to be $g = 9.81$ ms^{-2}, $f = 10^{-4}$ s^{-1}, respectively. The upper-layer and lower-layer thicknesses were taken to be $H_1 = 15$ m and $H_2 = 60$ m, and the density jump between the upper and lower layers was taken to be $\Delta\rho = 1.74$ kg m^{-3} with a reference density of $\rho_0 = 1000$ kg m^{-3}. The calculations follow the normal modes decomposition in the vertical direction [25], so that the barotropic (surface) horizontal free modes of oscillation are computed using the long wave speed for surfaces wave $c_{bt} = \sqrt{gH}$ where $H = H_1 + H_2$ is the total depth, and the baroclinic (internal, vertical mode 1) horizontal modes are computed using the long internal wave speed $c_{bc} = \sqrt{gH_e}$ where $H_e = (\Delta\rho/\rho_0)\, H_1 H_2/H$ is the equivalent depth. To facilitate a direct comparison, we have adopted Csanady's convention [25] of absorbing all of the stratification details into H_e, rather than defining a reduced gravity, g' as is usually done throughout this thesis. The importance of the density stratification relative to the Earth's rotation is captured by the non-dimensional quantity

$$S = \frac{c}{f r_0}\,, \tag{6.61}$$

known as the Burger number, that may be interpreted as the Rossby deformation radius, c/f, that has been non-dimensionalized by the basin length scale. The assumptions that underlie the normal modes decomposition are that finite amplitude (nonlinear) effects are negligible and that the bottom is flat. Although both barotropic and baroclinic modes are accessible using this technique, in this test case we present results for a subset of the baroclinic modes.

Since there are not any depth variations in this case, there will not be any rotational modes and all modes will be gravitational. In other words, it can be shown that the coefficients matrix $D = 0$. However, we do expect two distinct types of gravitational modes – a discrete finite number of Kelvin modes that are sub-inertial ($|\sigma/f| < 1$) and a countably infinite set of Poincaré modes whose frequencies are above the inertial frequency ($|\sigma/f| > 1$).

Kelvin modes may be further characterized by: (1) they decay exponentially away from the coastline (i.e., coastally trapped), and (2) the direction of propagation is counter-clockwise in the northern hemisphere (so-called right-bounded), and clock-wise in the southern hemisphere (left-bounded). It was first demonstrated by Lamb [71] that for circular basins, Kelvin modes are present whenever $S < 1/\sqrt{2}$. For the set of physical parameters described above, $S = 0.067 < 1/\sqrt{2}$, and we find that there are fourteen Kelvin modes.

	Current Method	Analytical	
s	σ/f	σ/f	Relative Error
1	0.069514	0.069418	0.0013844
2	0.13904	0.13883	0.0015106
3	0.20853	0.20824	0.0013735
4	0.27807	0.27764	0.0015312
5	0.34752	0.34703	0.0014061
6	0.41709	0.41641	0.0016186
7	0.48648	0.48577	0.0014589
8	0.55707	0.55512	0.0035239
9	0.6254	0.62444	0.0015399
10	0.69476	0.69375	0.001461
11	0.7643	0.76303	0.001665
12	0.83357	0.83229	0.0015304
13	0.9032	0.90153	0.0018462
14	0.9724	0.97075	0.0017009

Table 6.1: Analytical and numerical values for the non-dimensionalized frequencies (σ/f) of Kelvin modes with azimuthal mode number s in a stratified rotating basin with Burger number $S = 0.067$.

To verify the numerical method, we have compared analytically calculated Kelvin mode frequencies to those obtained numerically. The analytical calculations are obtained using a standard separation of variables technique, the details of which may be found in [25]. The resulting equation for the eigenvalues (i.e., frequencies) is in terms of Bessel functions, and thus the roots of these equations must be calculated numerically. This procedure was carried out using GNU Scientific Library (GSL) routines for rooting finding and evaluating the Bessel functions. Numerical calculations were carried out using a variety of grid parameters and expansion sizes for the streamfunction and velocity potential basis functions. In general, it is found that refining the mesh (i.e., adding more elements, K), for fixed polynomial order (N), and increasing the size of the bases all improved the agreement of the frequencies between the two methods. In the results below, the parameters were taken

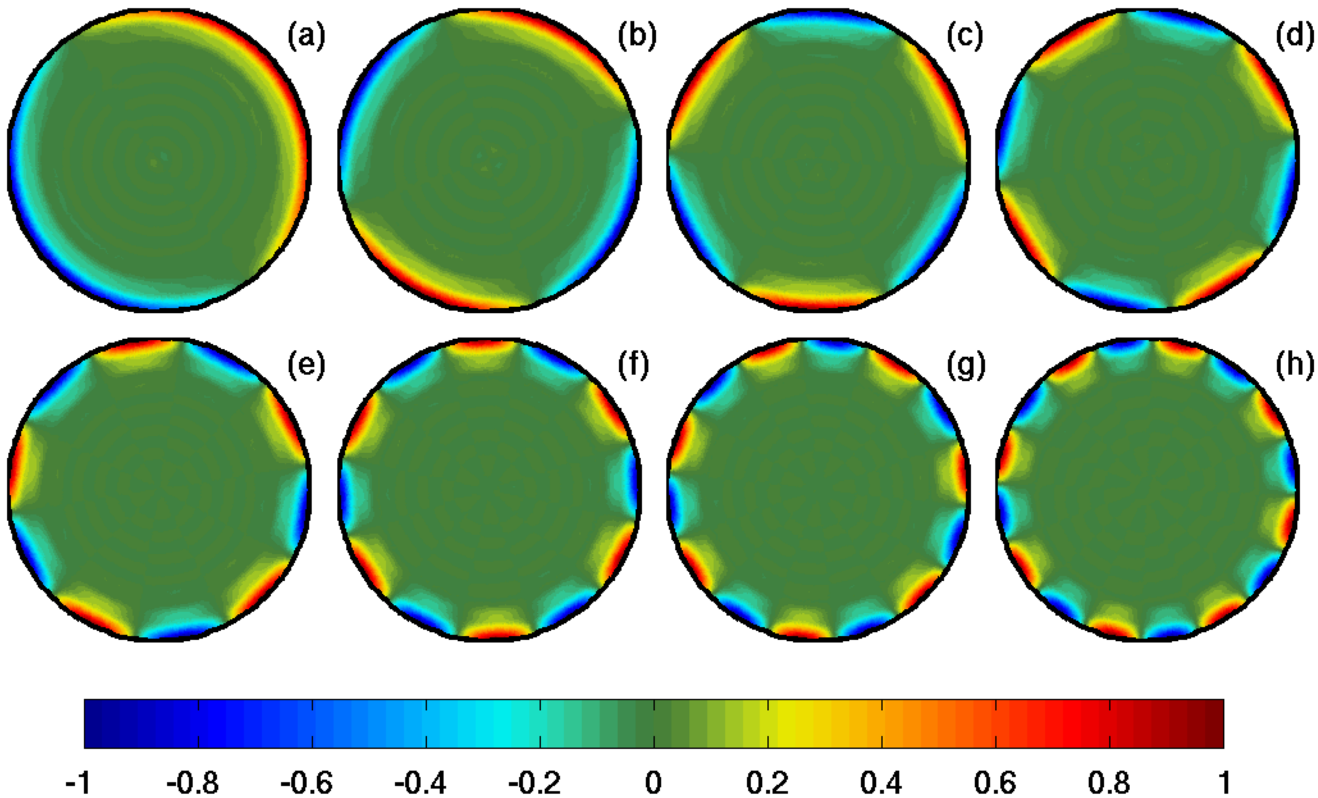

Figure 6.1: Numerically computed real part of the vertical mode-1 displacement, $\hat{\eta}_r$, for the first six Kelvin modes of a model large circular mid-latitude lake. The computed scaled frequencies (σ/f) for the modes shown in panels **(a)**–**(h)** are given in the first 8 rows in Table 6.1, respectively.

to be $N = 4$, $K = 710$, and $N_\phi = N_\psi = 200$. Table 6.1 lists the scaled Kelvin mode frequencies computed using both the analytical and numerical methods, along with the relative error. It is shown that the relative error in the computed Kelvin mode frequencies is $O(0.4\%)$ or less.

In Figure 6.1, the real parts of the spatial structure $(\hat{\eta}_r)$ of the first 8 numerically computed Kelvin modes are shown. In this case, we chose to plot the function $\hat{\eta}_r$, which may be interpreted as a snapshot of the interfacial displacement field taken at an arbitrary time, instead of plotting the amplitude and phase angles. We make this choice since the amplitudes $A(x, y)$ all carry the same structure for the Kelvin modes, and the phase angles $\theta(x, y)$ are highly irregular in regions away from the coastline where the amplitudes are negligible.

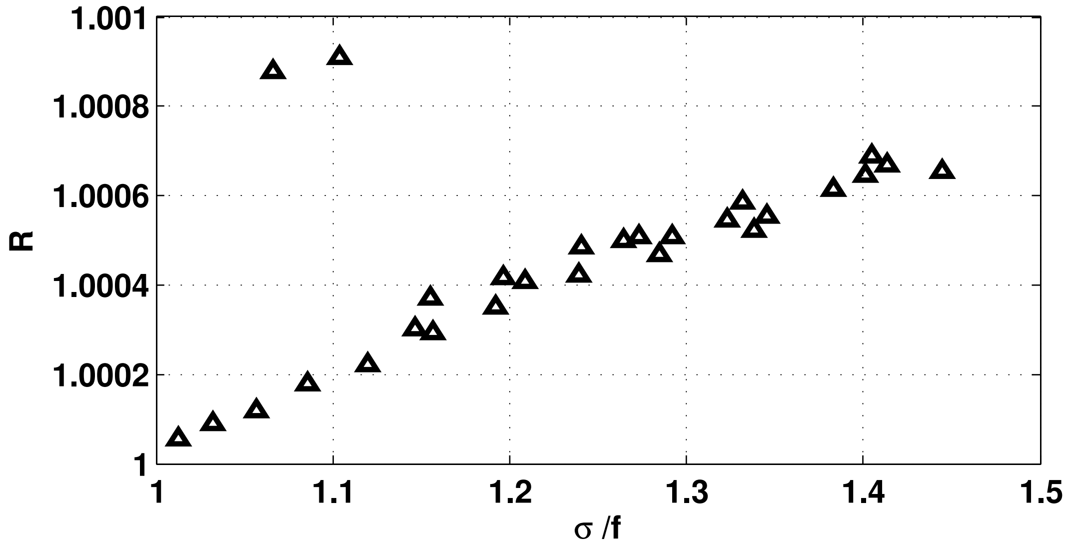

Figure 6.2: R, ratio of computed frequency to analytical frequency (i.e., $R = \sigma_{numerical}/\sigma_{analytical}$) vs. $\sigma_{analytical}/f$

In addition to Kelvin modes, we have also calculated a number of Poincaré modes and compared their frequencies to those computed analytically. The results are shown in Figure 6.2 where R, the ratio of computed frequency to analytical frequency, is plotted against the scaled analytically calculated frequency $\sigma_{analytical}/f$ for the first 28 Poincaré modes. Good agreement is found between the analytical and numerical methods since R does not exceed 1.001 for all modes considered here.

6.4 Validation – normal modes in a basin with parabolic bottom

The method remains to be validated in cases that involve variable depth where rotational modes exist, along with gravitational modes. To carry out such a validation, we refer to the analytical result of Lamb [71] for a circular basin with a parabolic bottom. The depth-profile is defined by

$$H(\mathbf{x}) = H_0 \left[1 - \left(\frac{r}{r_0} \right)^2 \right] , \tag{6.62}$$

where H_0 is the depth of the centre of the basin, r_0 is the radius of the lake and $r = \sqrt{x^2 + y^2}$. The fact that $H \to 0$ is problematic for the method described in Section 6.2 since the homogeneous eigenvalue problems (6.7) and (6.9) are singular at $r = r_0$ and the numerical eigenvalue solver used to construct the expansion bases does not converge. To side-step this difficulty, we perform our calculations on the perturbed depth profile $\tilde{H}(\mathbf{x}) = H(\mathbf{x}) + 0.005H_0$, under the assumption that such a small adjustment to the depth would not drastically alter the solutions. It was found that reducing the size of the perturbation polluted the spatial structure of the eigenmodes, and the frequencies converge to unreliable values. Examining the $\beta = 40$ case for the clockwise rotating mode with linear structure, it was found that decreasing the size of the perturbation caused the scheme to converge to an incorrect frequency of $\sigma/f = -1.0471$, while the correct frequency is $\sigma/f = -1.048$.

Lamb [71] lists frequencies for three values of the non-dimensional parameter $\beta = (fr_0/c_0)^2$, i.e., the square of the inverse Burger number with $c_0 = \sqrt{gH_0}$, and two specialized mode structures with azimuthal mode number $s = 1$. The radial structure of these modes is given by a terminating hypergeometric series. The first specialized mode has a linear radial structure, hence η is represented by a plane, and the second mode considered has a cubic structure in r. The plane mode appears twice in the set of modes, once as a clockwise rotating ($\sigma < 0$) gravity mode and once as a counter-clockwise rotating ($\sigma > 0$) rotational mode. The cubic mode, on the other hand, appears three times: once as a counter-clockwise rotational mode and also as a pair of counter-rotating gravity modes of different absolute frequency ($|\sigma|/f > 1$). The frequencies calculated by our method are compared to those given by Lamb in Table 6.2. Fair agreement of $O(1\%)$ or less is found in all cases except for the counter-clockwise cubic mode with $\beta = 40$ where the error was found to be $O(6\%)$. It is believed that the overall agreement is poorer in this case than for the Kelvin modes case (Section 6.3) since it was necessary to use a perturbed form of the depth profile used in the analytical solution, and the overall sensitivity of each mode to the perturbation for different β values is unclear.

s	Radial Structure	β	Current Method	Lamb (1932)	Relative Error
1	linear	2	-1.6229	-1.618	0.0030
			0.62366	0.618	0.0092
		6	-1.2658	-1.264	0.0014
			0.26657	0.264	0.0097
		40	-1.0476	-1.048	0.00038
			0.04837	0.048	0.0077
1	cubic	2	-2.9166	-2.889	0.0096
			0.62366	0.618	0.0092
			2.7912	2.764	0.0098
		6	-1.887	-1.874	0.0069
			0.10027	0.100	0.0027
			1.7858	1.774	0.0067
		40	-1.1801	-1.183	0.0025
			0.03757	0.040	0.0608
			1.1411	1.143	0.0017

Table 6.2: Comparison between scaled frequencies σ/f calculated using the present method and the analytical results of [71] for the free modes of oscillation in a circular lake with parabolic bottom. The parameter s is the azimuthal mode number, and β is the square of the inverse Burger number, i.e., $(fr_0/c_0)^2$.

6.5 Comparison with simulations: Kelvin waves on a model large circular mid-latitude lake

The method discussed above can also be thought of as a validation tool for numerical simulations of shallow water models where closed-form analytical solutions are not available. It can also be used to help interpret simulation results by determining which free modes of oscillation have been excited in the solution. In this section, we initialize the one-layer DG-FEM model from Chapter 4 with the super-position of the real part of the first three Kelvin modes from Csanady's large circular mid-latitude lake, shown in Figure 6.1**(a)**–**(c)**. The initial velocity $\mathbf{u}$ of the vertical mode-1 Kelvin waves were recovered from the stream-function and potential using the Helmholtz decomposition (6.3). The initialization thus takes the form

$$\begin{pmatrix} \eta_0 \\ \mathbf{u}_0 \end{pmatrix} = \sum_{i=1}^{3} \begin{pmatrix} \eta^{(i)} \\ \mathbf{u}^{(i)} \end{pmatrix} , \tag{6.63}$$

where superscript (i) represents the i^{th} gravitational mode. Here, each mode $(\eta^{(i)}, \mathbf{u}^{(i)})^\mathsf{T}$ has been scaled such that $\max(\eta^{(i)}) = 10^{-5} H_e$ so that nonlinear effects would be negligible. The order $N = 4$ DG-FEM method was used along with the same $K = 710$ element triangular mesh used to compute the modes. The solution was integrated out to 4 periods of the lowest frequency Kelvin wave.

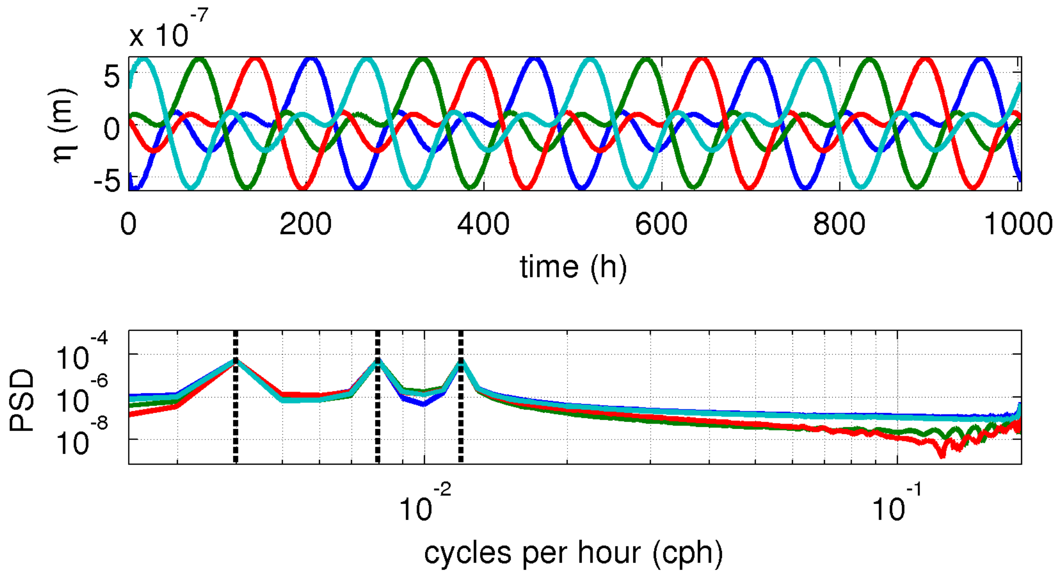

Figure 6.3: Top: Time series taken of η from the 'Kelvin waves on a model large circular mid-latitude lake' simulation taken at the points $(x, y) = (0, r_0)$ (blue), $(0, -r_0)$ (green), $(r_0, 0)$ (red), $(-r_0, 0)$ (cyan). Bottom: Corresponding power spectral density for each of the curves in the top panel. Dashed curves represent theoretical frequencies of the first three Kelvin modes with calculated periods of $T = 251$ h, $T = 125.5$ h, and $T = 83.7$ h.

In Figure 6.3, we plot the time series and corresponding power spectral density of the interfacial displacement η at the four points corresponding to the ends of the basin in the four compass directions. We find that the spectral analysis recovers the theoretically predicted frequencies of the three Kelvin waves quite well, since the three peaks in the spectrum coincide directly with the calculated periods of $T = 251$ h, $T = 125.5$ h, and $T = 83.7$ h.

6.6 Normal modes in a lake with a wavy coastline

In this section, we revisit the idealized basin considered in Section 4.12 that represents a rose-petal-like perturbation on the classical circular geometry. Here, we choose the same physical parameters used in Chapter 4. The Coriolis frequency is given by $f = 7.8828 \times 10^{-5}\ \mathrm{s}^{-1}$, the depth is $H = 12.8$ m, and the reduced gravity is $g' = 0.024525$ m s^{-2}. Given that the typical length scale is $r_0 = 8345$ m, the Burger number in this case is $S = 0.852$.

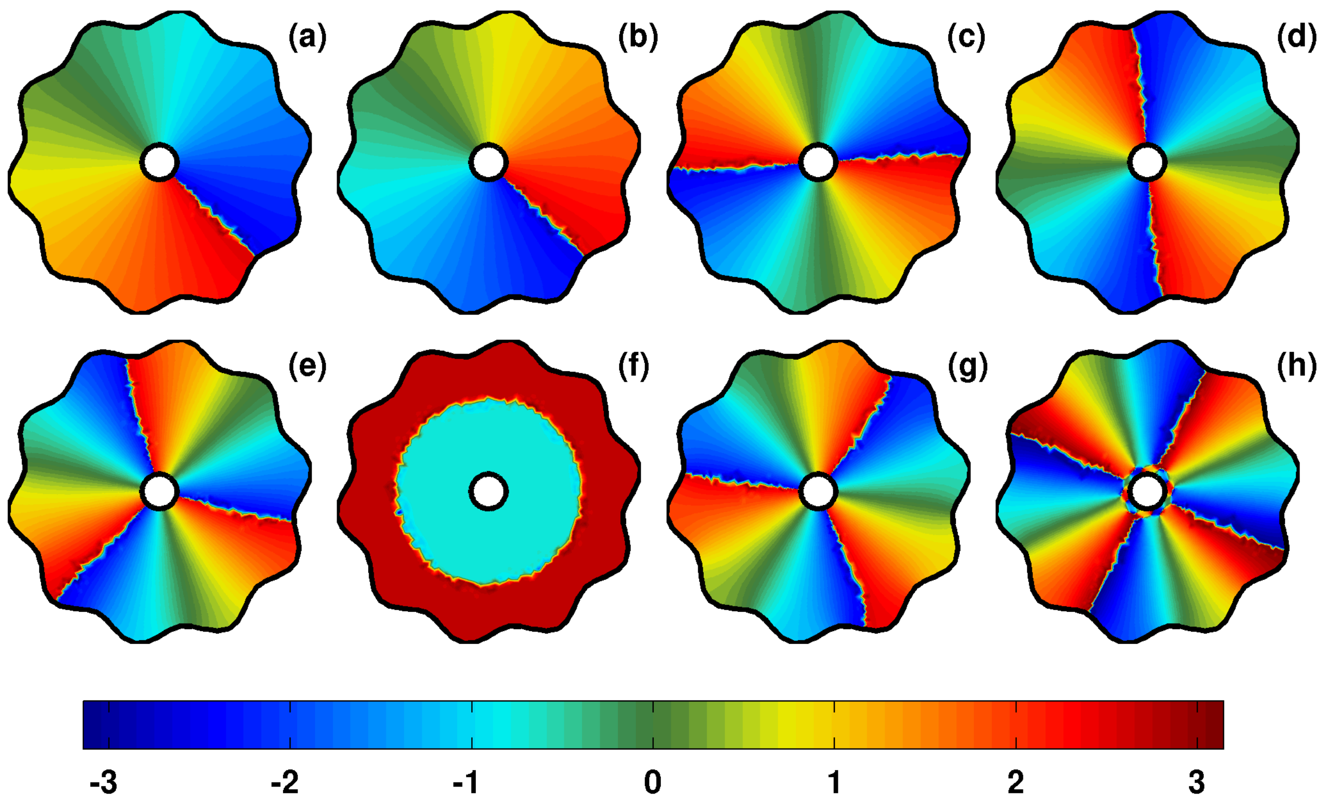

Figure 6.4: Phase angles $\theta(x, y)$ of 8 gravitational modes of the model lake with a wavy coastline. The corresponding periods of the modes are given by **(a)** $T = 18.21$ h, **(b)** $T = 11.26$ h, **(c)** $T = 9.89$ h, **(d)** $T = 7.37$ h, **(e)** $T = 6.97$ h, **(f)** $T = 6.45$ h, **(g)** $T = 5.71$ h, **(h)** $T = 5.49$ h.

The free modes of oscillation were computed using the $K = 1330$ element mesh used previously for this geometry with polynomial order $N = 4$ and $N_\psi = N_\phi = 200$ basis

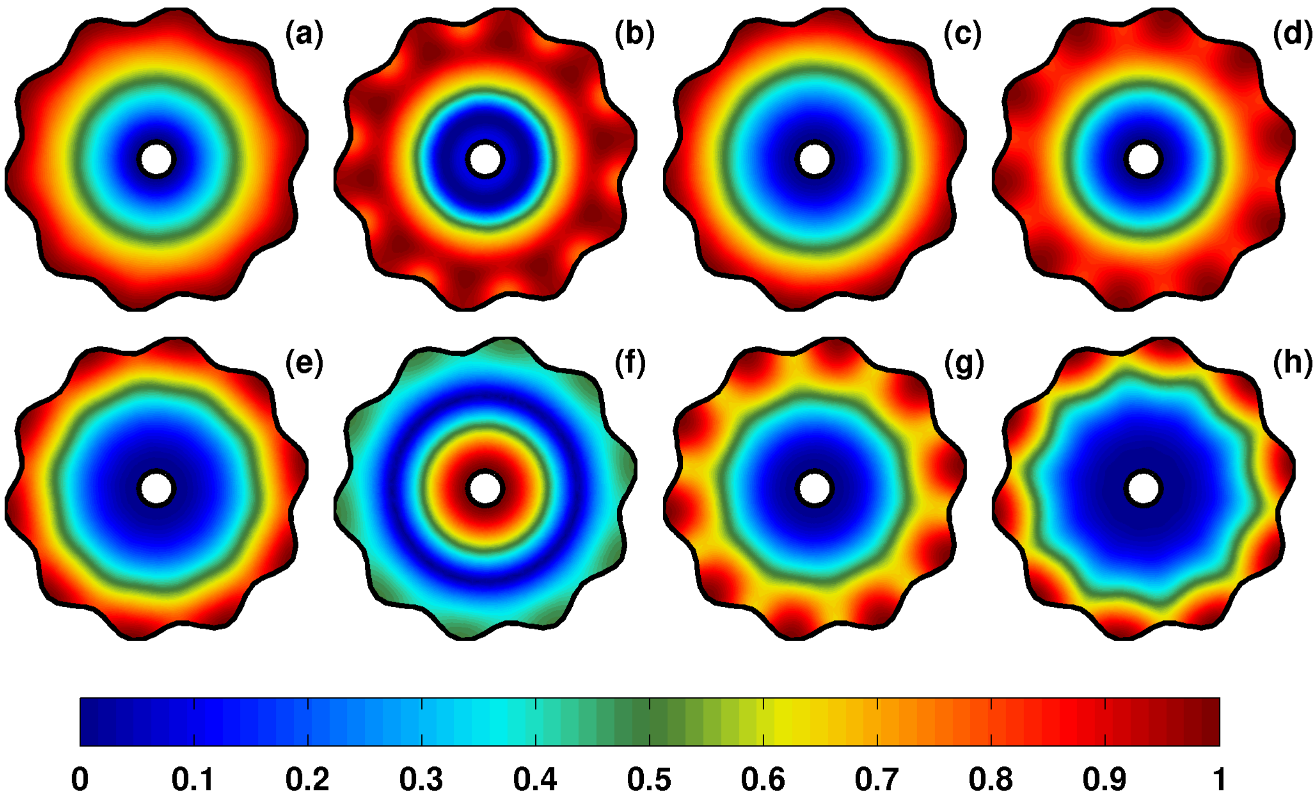

Figure 6.5: Like Figure 6.4, but the amplitude $A(x, y)$ is plotted. $A(x, y)$ is scaled to have a maximum value of 1.

functions. The phase angles $\theta(x, y)$ and amplitudes $A(x, y)$ of the first 8 free modes of oscillation are presented in Figures 6.4 and 6.5, respectively. The plotted modes have periods between 18.21 h and 5.49 h, all of which are below the inertial period since the lowest frequency mode has $\sigma/f = 1.22 > 1$. Hence, these modes can be thought of as Poincaré waves [70, 115].

Recalling that high water propagates in the direction of increasing θ, we find that the first four free modes (Fig. 6.4 **(a)**–**(d)**) appear in counter-rotating pairs of different frequency with the lowest frequency mode rotating counter-clockwise. Interestingly, a radially-symmetric mode (panel **(f)**) appears between the azimuthal mode-3 pair (panels **(e)** and **(g)**). The azimuthal mode-4 mode (panel **(h)**) shows a small cell near the centre island that is out of phase with the dominant outer motion, though both propagate counter-clockwise. Inspecting the amplitudes in Figure 6.5, we find that nodal points

($A = 0$) typically occur at or near the centre of the basin for these large-scale modes, except in the case of the radially symmetric mode (panel **(f)**). The different concentrations of amplitude along the outer coast are also worth noting, with some modes showing stronger intensification in the small dimples or 'bays.'

6.6.1 Effects of stronger rotation

To illustrate the impact of stronger planetary rotation (or equivalently, weaker stratification), we have re-computed the free modes of oscillation on the same basin considered in the above section but f has been increased to $f = 1.4554 \times 10^{-4}\ \mathrm{s}^{-1}$ (North Pole rotation) and $f = 10^{-3}\ \mathrm{s}^{-1}$ (an artificially high value) such that the corresponding Burger numbers are $S = 0.462$ and $S = 0.067$. In Figure 6.6, we show a comparison between the amplitudes of the lowest frequency gravity modes for $S = 0.852$ (same as Figure 6.5 **(a)**) and these two new values for the Burger number. In Figure 6.6 **(b)**, we see that increasing the Burger number to $S = 0.0462$ has decreased the scaled frequency from $\sigma/f = 1.22$ to $\sigma/f = 0.581$, but only slightly altered the amplitude distribution such that the $O(1)$ values of $A(x, y)$ are shifted closer to the outer coastline. Decreasing S to 0.067 in panel **(c)** causes the mode to be highly trapped along the outer coastline and its scaled frequency decreases to $\sigma/f = 0.0652$.

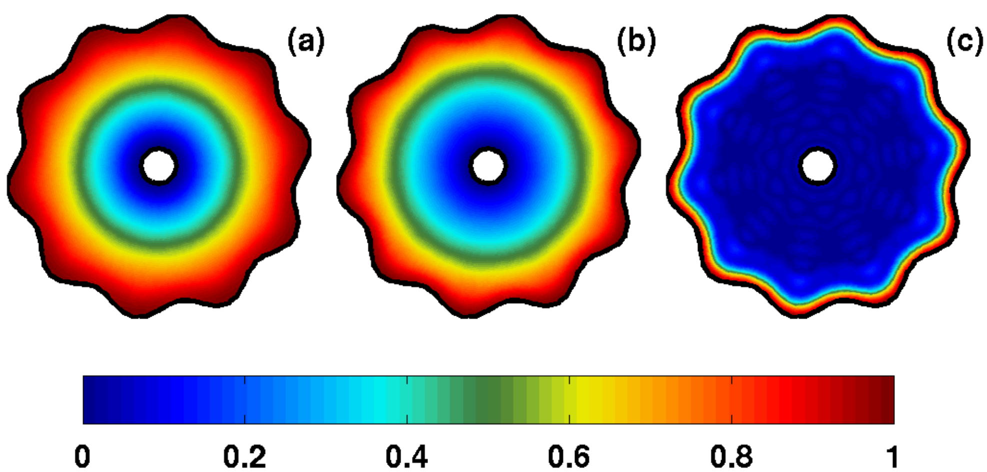

Figure 6.6: Amplitudes $A(x, y)$ of the lowest frequency modes on the lake with a wavy coastline and varying Burger numbers S. Each panel corresponds to **(a)** $S = 0.852$, $\sigma/f = 1.22$, **(b)** $S = 0.462$, $\sigma/f = 0.581$, **(c)** $S = 0.067$, $\sigma/f = 0.0652$.

The value $S = 0.067$ corresponds to the same value of S as Csanady's model large circular mid-latitude lake in Section 6.5, and the mode pictured in panel **(c)** is analogous to an azimuthal mode-1 Kelvin wave on a circular basin. The results shown here illustrate the transition of the lowest frequency free mode of oscillation on a nearly circular basin from the super-inertial $|\sigma/f| > 1$ to the sub-inertial $|\sigma/f| < 1$ frequency regimes. In other words, the mode transitions from a Poincaré wave to a Kelvin wave. While the results shown here indicate that the lowest frequency mode always possesses azimuthal mode-1 shape and rotates counter-clockwise, the effect of increased rotation (or decreased stratification) tends to increase the extent to which the mode is trapped along the outer coastline, i.e., to behave more like a Kelvin wave propagating along a straight and infinite coast.

6.6.2 Effects of variable bathymetry

Up until this point, we have focused purely on lakes with a flat bottom, that is $H = const.$ We now turn our attention to the effects of bottom topography on the free modes of oscillation in the same idealized geometry as above, but we define the depth profile as

$$H = H_0(3 - \tanh(x/\lambda))/4 \; , \tag{6.64}$$

with $H_0 = 12.8$ m and $\lambda = 2$ km, such that the depth decreases by a factor of two (from $H = 12.8$ m to $H = 6.4$ m) across a thin transition region centred about $x = 0$. The linear modes calculation was carried out with $N_\phi = N_\psi = 300$ basis functions and the mesh and polynomial order were taken to be the same as in previous sections: $(N, K) = (4, 1394)$. Figures 6.7 and 6.8 plot the amplitudes and phases of the first 6 gravitational modes, respectively. Here, the Burger number is $S = \sqrt{g'\overline{H}}/fr_0 = 0.7376$, where $r_0 = 8345$ m, $\overline{H} = 9.6$ m, $g' = 0.0025g = 0.025$ ms^{-2} and $f = 7.8828 \times 10^{-5}$ s^{-1}.

Figures 6.7 and 6.8 should be compared and contrasted with the flat bottom case shown previously in Figures 6.4 and 6.5. A main result is that the amplitude of each mode tends to be stronger at the eastern end of the basin where the depth is lower. Furthermore, nodal points appear to be shifted to the right, whereas many of the modes in the flat bottom case were centred about $(x, y) = (0, 0)$. Comparing the phase angle plots, the breaking of symmetry due to changes in depth is a clearly evident aspect of the results (see for example, panel **(e)**), and such an effect is indicative of the fact that wave refraction plays an important role in dictating the spatial structure of the modes. More rapid phase changes in shallow water than in deep water are visible as well.

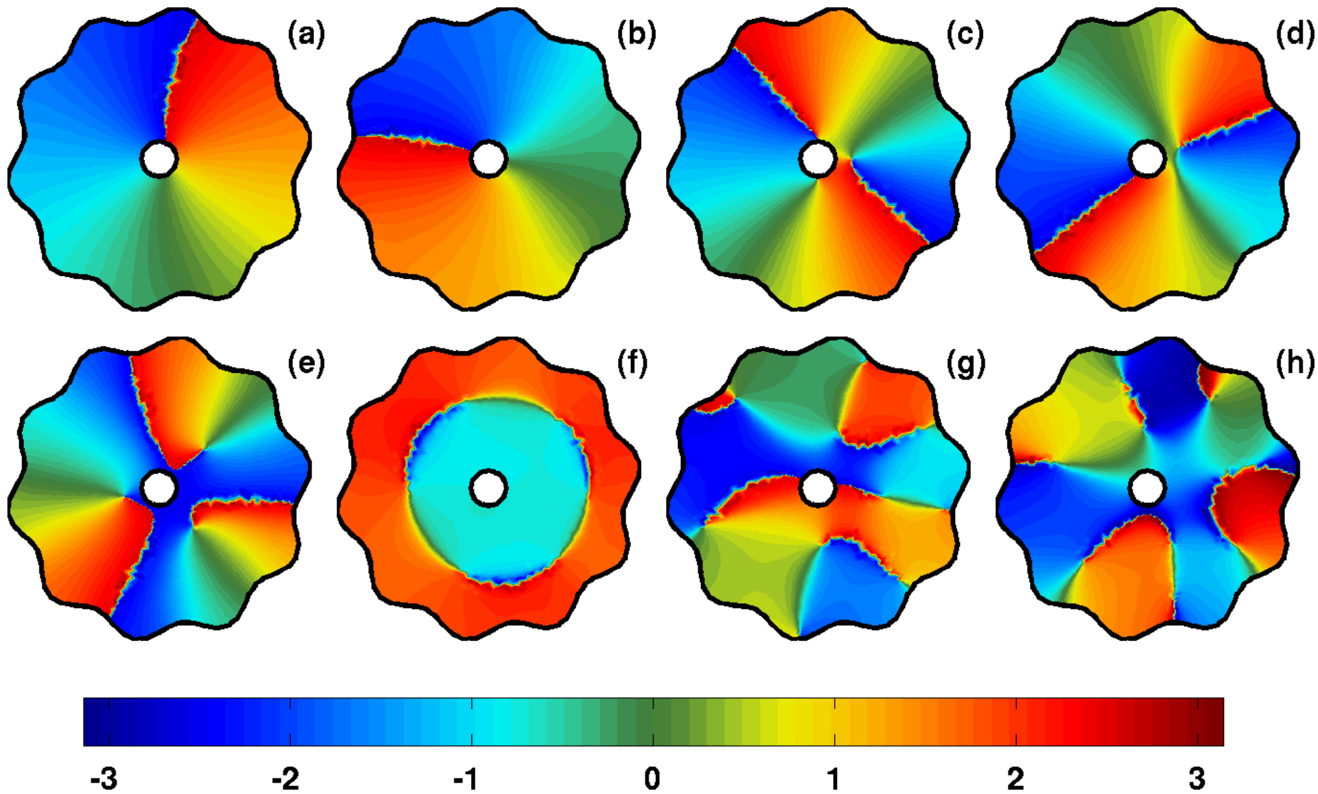

Figure 6.7: Phase angles $\theta(x, y)$ of 8 gravitational modes of the model lake with a wavy coastline and variable bathymetry. The corresponding periods of the modes are given by **(a)** $T = 22.41$ h, **(b)** $T = 12.79$ h, **(c)** $T = 12.09$ h, **(d)** $T = 8.58$ h, **(e)** $T = 8.50$ h, **(f)** $T = 7.78$ h, **(g)** $T = 6.83$ h, **(h)** $T = 6.62$ h.

Rotational modes

In addition to rotating gravity modes, 150 distinct rotational modes were calculated using the method. This is the first occurrence of rotational modes presented thus far, and in the absence of a variation in the Coriolis parameter, the presence of such modes is solely due to a non-flat bottom. Here, we choose the mode with the largest spatial structure for examination. Since it has the largest structure, it is presumed to be the most important rotational linear mode in the physics of the model lake considered in this section because it would be forced by large scale wind patterns.

In Figure 6.9, snapshots of $\Re(\eta)/\max_{x,y}(|\hat{\eta}|)$ are shown at fixed times spanning one full

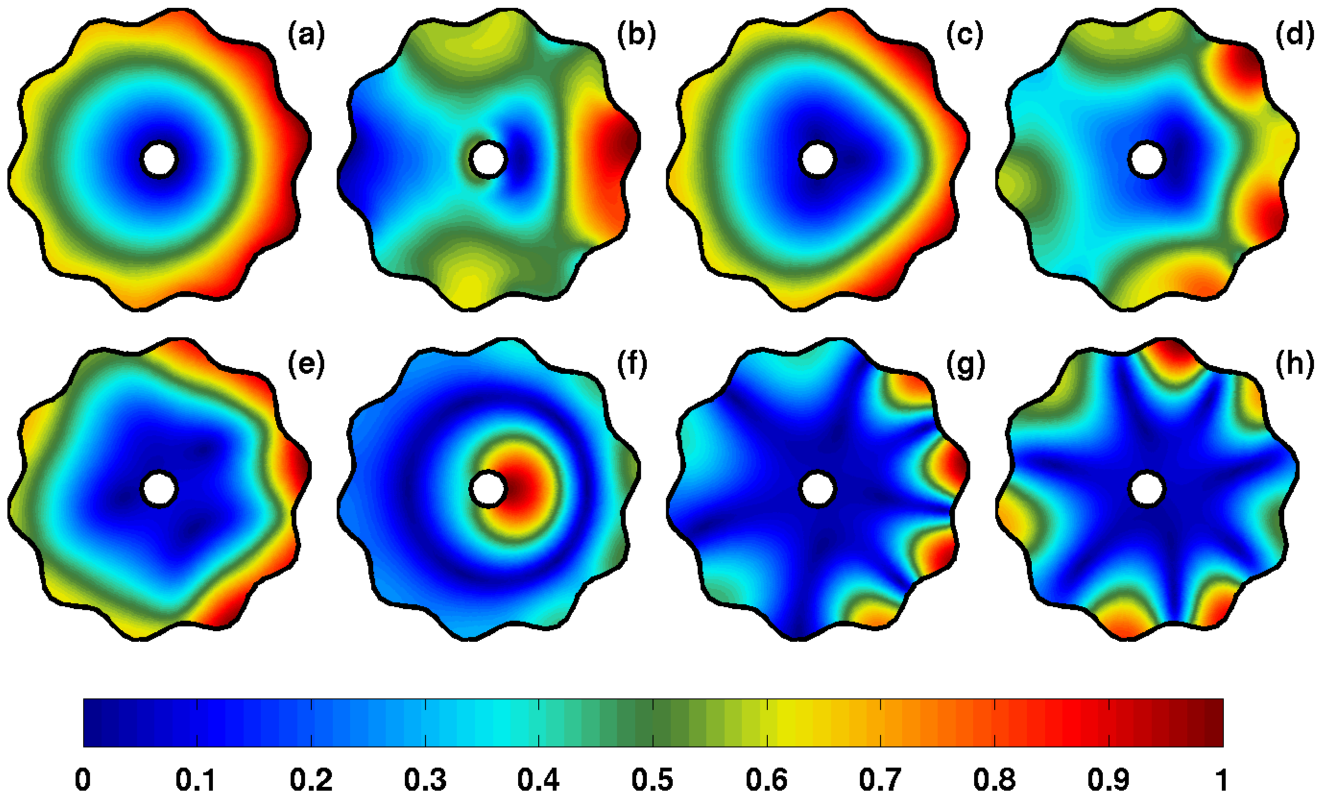

Figure 6.8: Like Figure 6.7, but the amplitude $A(x, y)$ is plotted. $A(x, y)$ is scaled to have a maximum value of 1.

wave period of $T = 195.6$ h. The mode behaves as a topographically trapped wave that propagates along the region centred about $x = 0$, where the gradient of the depth profile is highest. The existence of such a wave is analogous to 'Rossby waves' on the beta plane [92, 70]; westward propagating vorticity waves that exist due to a northward gradient in planetary vorticity. The mode depicted in Figure 6.9 is a northward propagating wave that exists due to an eastward (positive x) depth gradient that corresponds to a westward gradient in potential vorticity. Due to this analogy, these waves have been referred to as 'topographic Rossby waves' [116]. The traditional (non-dispersive) shallow water model guarantees that potential vorticity defined by $q = (\zeta + f)/H$ is conserved following the flow [92], i.e.,

$$\frac{Dq}{Dt} = 0 , \tag{6.65}$$

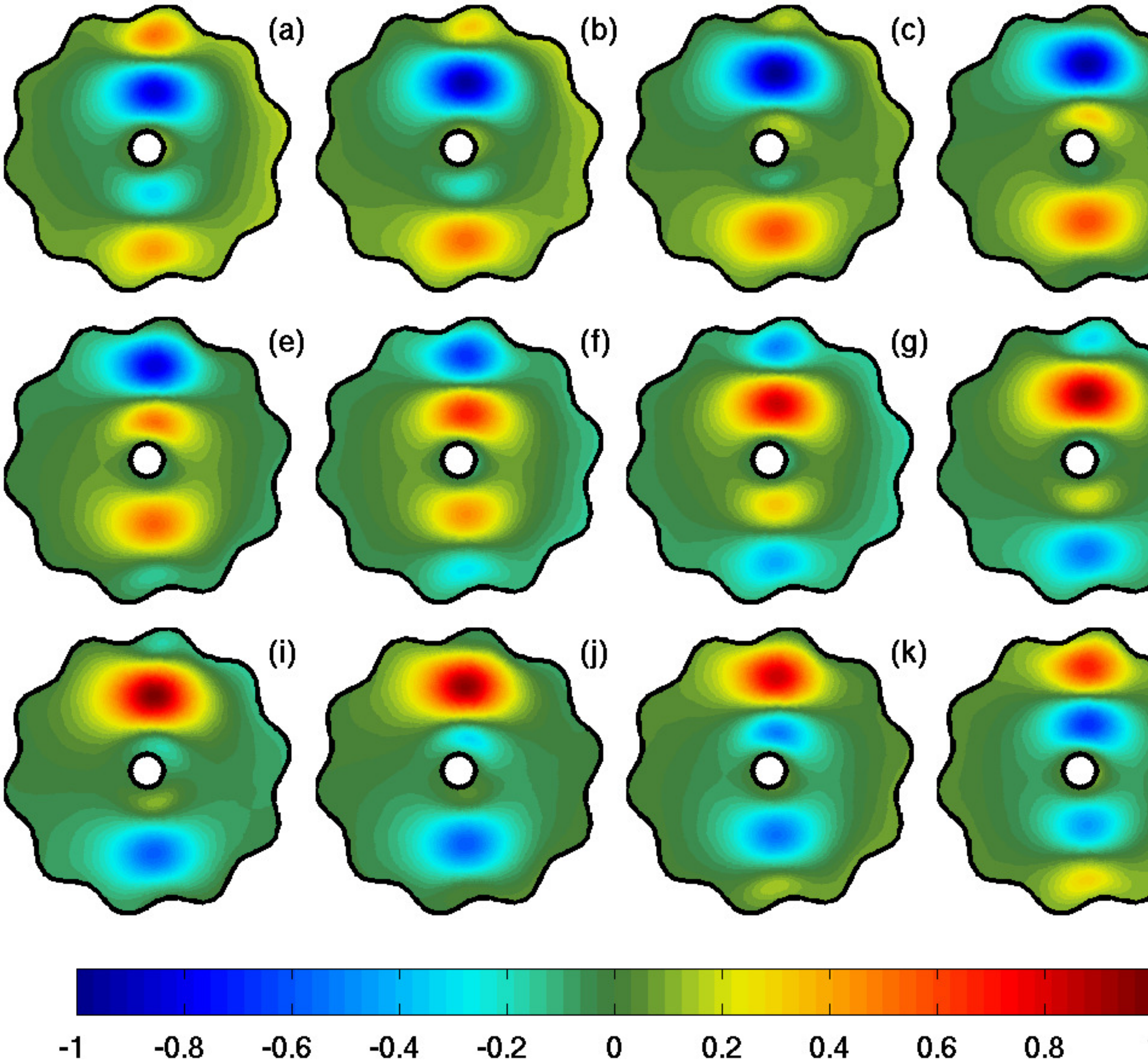

Figure 6.9: Snapshots of one full wave period of $\Re(\eta)/\max_{x,y}(|\hat{\eta}|)$ of the largest scale rotational mode computed in the perturbed circular basin with variable bathymetry. The times of each panel are given by **(a)** $t = 0$, **(b)** $t = 0.083T$, **(c)** $t = 0.167T$, **(d)** $t = 0.25T$, **(e)** $t = 0.333T$, **(f)** $t = 0.417T$, **(g)** $t = 0.5T$, **(h)** $t = 0.583T$, **(i)** $t = 0.667T$,**(j)** $t = 0.75T$, **(k)** $t = 0.833T$,**(l)** $t = 0.917T$. Here, $T = 195.6$ h.

where $\zeta = v_x - u_y$ is the relative vorticity.

6.7 Comparison with simulations: Poincaré waves on a lake with a wavy coastline

In this section, we carry out a simulation where we initialize the single-layer model from Chapter 4 on the lake with a wavy coastline discussed in Section 4.12 with the lowest frequency gravity mode, and we scale its maximum amplitude to $a = 10^{-5}H$ so that non-linear effects are negligible. It is assumed that since the mode is large-scale, that dispersive effects should be negligible as well and the model should behave as the linear shallow water equations. The model was initialized with the real part of the lowest frequency mode with period $T = 18.21$ h. The phase angle and amplitude of this mode is depicted in Figures 6.4 **(a)** and 6.5 **(a)**, respectively. The simulation was time-stepped to $t = 182$ h, or ten periods of the lowest frequency mode.

Here, in Figure 6.10 **(a)**, we plot the time series of the interfacial height η as measured from four points throughout the basin. The corresponding power spectral density is shown in panel **(b)**, where the most prominent peak in all curves agrees quite well with the frequency predicted from the linear theory calculation, and there do not appear to be any other well-defined peaks in the spectrum.

In Figure 6.11, the effects of nonlinearity are explored for the same geometric configuration by increasing the maximum amplitude of the initial η to $a = 0.1H$. The initial velocity has been re-scaled appropriately as well. We have time-stepped the equations for four periods of the lowest frequency mode, or twice as long as in Figure 6.10. We once again find that the most prominent peak in all power spectral curves corresponds to the lowest frequency predicted by the linear theory calculation. For the time series taken near the outer coastline, we find that nonlinear effects have excited a number of other peaks in the spectrum. We do not find these same peaks for the cyan curve that is taken near the inner island due to the fact that nonlinear steepening is localized along the outer coast, and the dynamics in the centre of the basin remain essentially linear. It is worth noticing that for the timescale of the simulation carried out here, the peaks excited due to nonlinearities do not appear to directly coincide with the frequencies of the modes predicted by linear theory. Snapshots of the evolving η field are shown in Figure 6.12 to illustrate the effects of local nonlinear steepening on the basin-scale wave. If the dynamics were purely linear, all panels would be identical to the initial condition (panel **(a)**) since the times in panels **(b)**–**(d)** are given at integer multiples of the mode's period. Instead, there is a clear

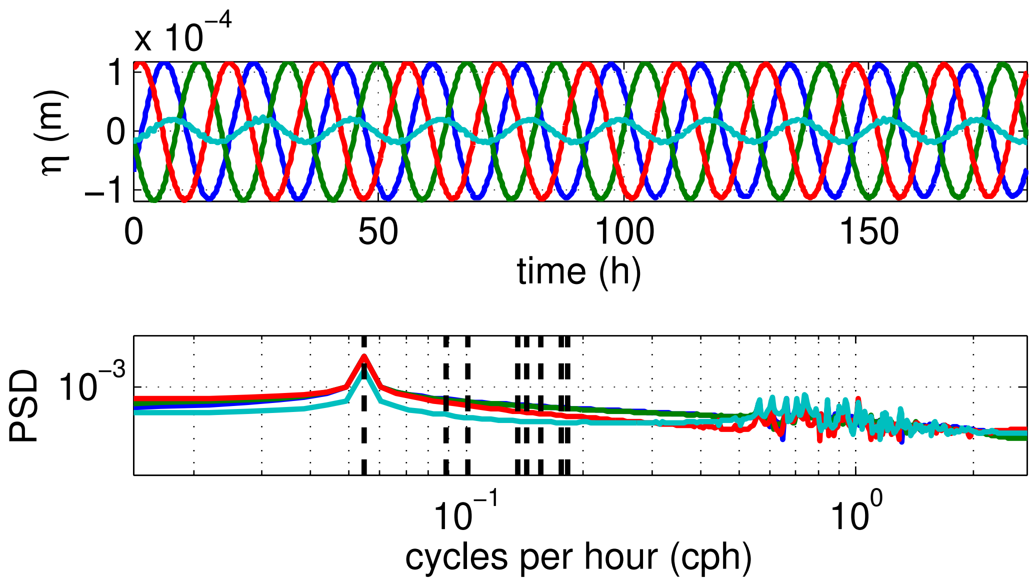

Figure 6.10: Panel **(a)**: Time series of η for a simulation initialized with the lowest-frequency Poincaré mode at the points shown in Figure 4.8 **(b)**. The blue, green, and red curves correspond to points near the outer coastline, while the cyan curve corresponds to a point near the centre island. The corresponding power spectral density is shown in panel **(b)** where the dashed vertical line represents the predicted frequency of 0.0549 cph (or $T = 18.21$ h).

steepening of the wave visible in panels **(b)** through **(d)**. This steepening preferentially occurs along the leading edge of the wave front, becoming more pronounced with each wave period, and it is clear by contrasting with Figure 6.5 that it does not project onto any of the first eight Poincaré modes in a clean manner.

In light of the above discussion, it is worth exploring whether one of these clockwise harmonics would remain coherent if a simulation was initialized with one. Such a case is considered in Figure 6.13 where we initialize with the Poincaré mode with the 4th lowest frequency, a mode that exhibits clockwise rotation (see Figure 6.4 **(d)**) with period $T = 7.37$ h. The simulation was time-stepped to $t = 29.48$ h, or four modal periods. In direct analogy with the results presented in Figure 6.10, we find a single peak in the spectrum that corresponds precisely to the frequency of the mode used to initialize the simulation.

In Figure 6.14, we consider the question of which gravity modes would be excited by an initial condition corresponding to a linear east-west tilt in the interface with no initial

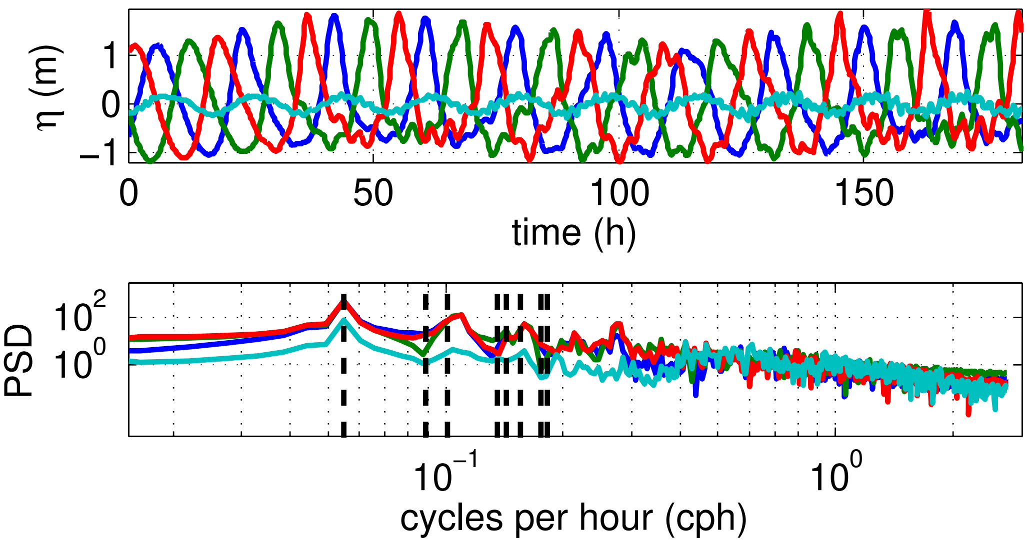

Figure 6.11: Like Figure 6.10, but the amplitude has been increased to $a = 10^{-1}H$ and the integration time has been doubled. The dashed lines correspond to the theoretically predicted frequencies of the first 8 modes.

velocity. Nonlinear effects were once again suppressed by taking the maximum amplitude to be $a = 10^{-5}H$. In this case, the time series plots suggest that the solution is comprised of the superposition of many modes since we do not observe simple sinusoidal wave forms as we did when we our initialization consisted of one or more of the modes themselves. The power spectra suggest that the two lowest frequency modes, both of azimuthal mode 1 shape, have been excited. Here, the second lowest mode rotates clockwise. Contrary to the other time series, the time series taken near the centre island (cyan curve) shows a stronger peak at the second mode than the first mode. This observation agrees with the fact that the amplitude $A(x, y)$ is lower at the centre island for the first mode than the second mode (cf. panels **(a)** and **(b)** of Figure 6.5). It appears that the third gravitational mode (counter-clockwise, azimuthal mode 2) may have been excited as well, however it is not as clear as for the first two modes.

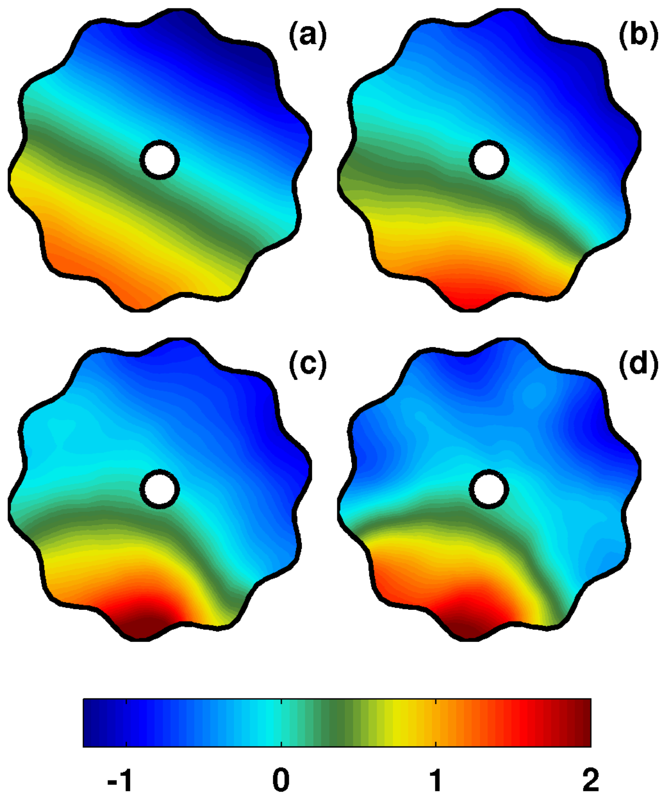

Figure 6.12: Snapshots of the η field from the simulation initialized with the lowest gravity mode and maximum amplitude $a = 0.1H$ at **(a)** $t = 0$, **(b)** $t = T$, **(c)** $t = 2T$, **(d)** $t = 3T$, where $T = 18.2$ h is the period of the mode as predicted from the linear theory calculation.

6.8 Free modes of oscillation in Pinehurst Lake, AB

We next return to the situation considered in Section 4.16 of Pinehurst Lake, Alberta. The mesh and bathymetry data used here are the same as those in Figure 4.15, and the physical parameters were taken to be the same as previously: $g' = (\Delta\rho/\rho_0)g = 0.024525$ m s^{-2}, where $(\Delta\rho/\rho_0) = 0.0025$, and $f = 1.1863 \times 10^{-4}$ s^{-1}. We have opted to use the same parameters as the simulation reported on in Chapter 4, since the details from the calculated modes may help to shed further light on the results of the simulation considered there. A rough estimate for the Burger number is $S \approx \sqrt{g'\overline{H}}/(f\sqrt{A}) \approx 0.74$, where $A = 39.0$ km^2 is the area of the basin and $\overline{H} = 12.4$ m is the mean depth, both were computed numerically.

The phase angles and amplitudes of the first 8 modes are shown in Figures 6.15 and 6.16,

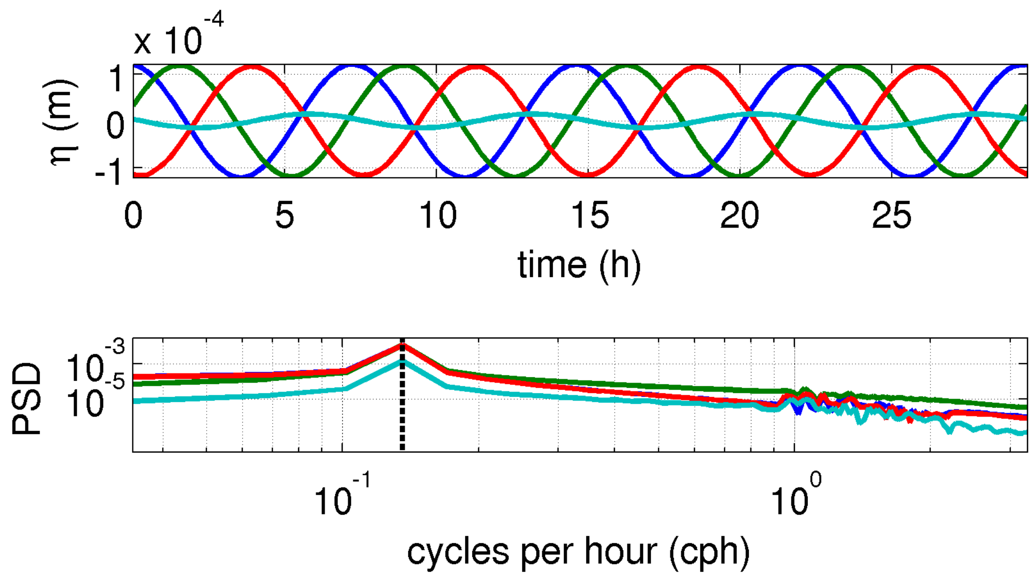

Figure 6.13: Like Figure 6.10, but the initial condition was taken to be the 4^{th} lowest frequency Poincaré mode with maximum amplitude $a = 10^{-5}H$. The dashed line corresponds to the theoretically predicted period of $T = 7.37$ h.

respectively. Unlike in the geometrically simpler case of the perturbed circular basin considered in Section 6.6, we do not simply find pairs of counter-rotating modes of different frequency and slightly different spatial structure since the basin's geometric complexity breaks the majority of the modes into smaller cells that exhibit their own local rotation/propagation properties. The exception is the lowest frequency mode shown in panel **(a)** with period $T = 12.84$ h. This mode exhibits basin-wide counter-clockwise rotation about a single nodal point near the centre of the basin.

Inspecting the amplitudes of the various basin modes in Figure 6.16, we notice that the regions of highest amplitude are typically found in confined, narrow bays, especially in the shallows in the eastern part of the basin. This result provides insight on the simulation presented in Section 4.16 where it was found that the seiche-induced flow past coastal obstacles was intensified by geometric focusing in narrow and confined parts of the basin. Such energy focusing coincides well with the excitation of the various low frequency modes as predicted by the linear theory calculation.

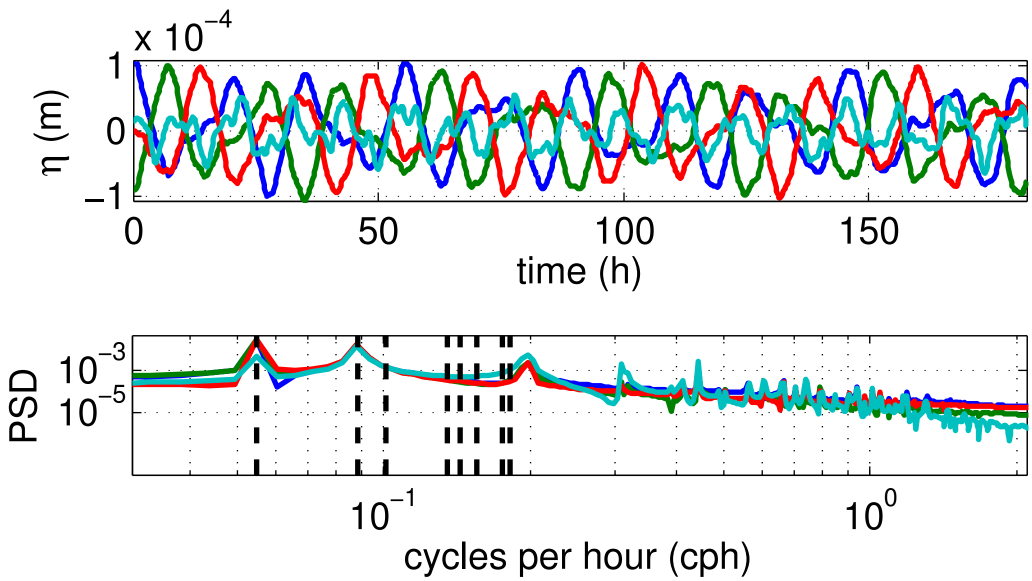

Figure 6.14: Like Figure 6.11, but the intial condition was taken to be an east-west linear tilt with maximum amplitude $a = 10^{-5}H$.

6.9 Discussion and conclusions

In this chapter, the calculation of the free modes of oscillation in arbitrarily shaped, closed basins with rotation was considered, and the modes themselves were studied. As explained in previous works, [99, 100], the standard Laplace equation eigenvalue problem obtained in the absence of rotation, no longer holds when rotation is included, and hence the inclusion of f-plane rotation complicates the calculation considerably. As a result, both Helmholtz and Galerkin decomposition techniques are required to recover a self-adjoint matrix eigenvalue problem for the unknown frequencies and Galerkin projection coefficients of the free modes of oscillation. In this work, the continuous differential operators have been discretized using the symmetric interior penalty discontinuous Galerkin (SIP-DG) method that was introduced previously in Chapter 4. The SIP-DG method allows for the construction of basis functions from discretized generalized eigenvalue problems that are specified in terms of symmetric matrices.

Once the linear free modes of oscillation are calculated for a given physical situation, two key questions arise. Firstly, are these modes generated in field situations when driven by wind forcing? Secondly, do the modes persist in the basin-scale physics once generated? In this chapter, we have primarily focused on the second question and have found that if

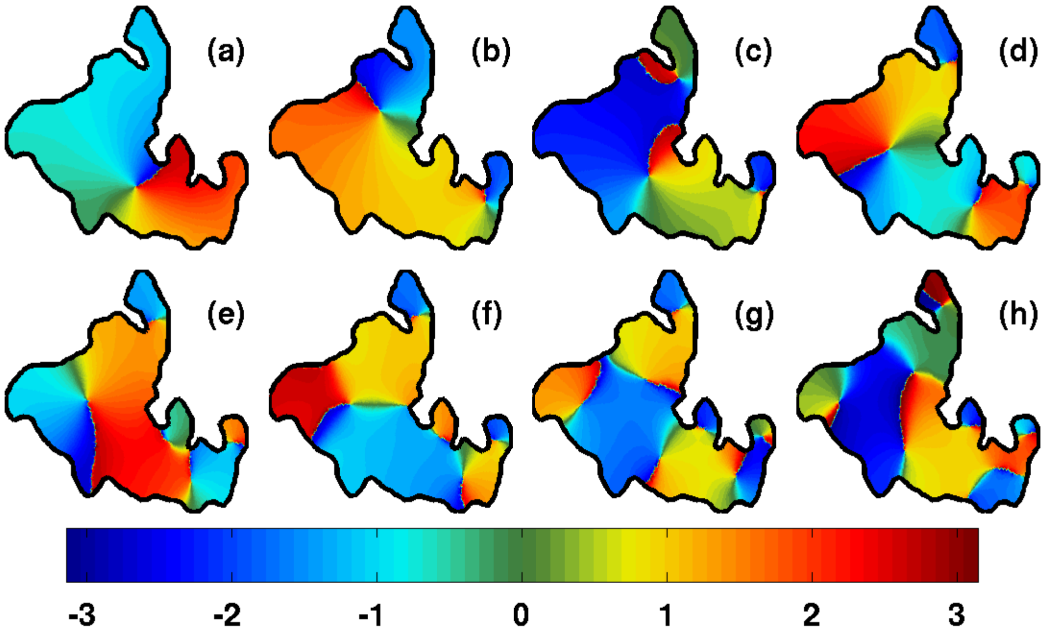

Figure 6.15: Phase angles $\theta(x, y)$ of the lowest 8 gravitational modes of Pinehurst Lake. The corresponding periods of the modes are given by **(a)** $T = 12.84$ h, **(b)** $T = 9.57$ h, **(c)** $T = 7.66$ h, **(d)** $T = 5.67$ h, **(e)** $T = 5.00$ h, **(f)** $T = 4.45$ h, **(g)** $T = 3.67$ h, **(h)** $T = 3.24$ h.

a simulation is initialized with a mode (or linear super-position of modes) then the mode remains intact throughout the simulation as long as nonlinear (finite amplitude) effects are negligible. In simulations where nonlinear effects were prevalent, low frequency modes were found to steepen and lead to the excitation of higher-frequency modes. It was also found that there were nonlinearly excited peaks in the power spectra that did not directly match any of the frequencies from linear theory. Question (1) could be the subject of future work and could be explored either by including a wind-forcing parameterization in the model simulations or by including forcing terms in the decomposition problem.

The method has been used to investigate the effects of rotation and variable bathymetry in a simple model lake. It was found that stronger rotation tends to introduce modes that are trapped along the coast. This observation is consistent with the theoretical predictions for the channel geometry (see 2.4.1). Variable bottom bathymetry, on the other hand, modifies gravity modes by enhancing their amplitude in more shallow regions. Variable bathymetry also causes a potential vorticity gradient in the background state that intro-

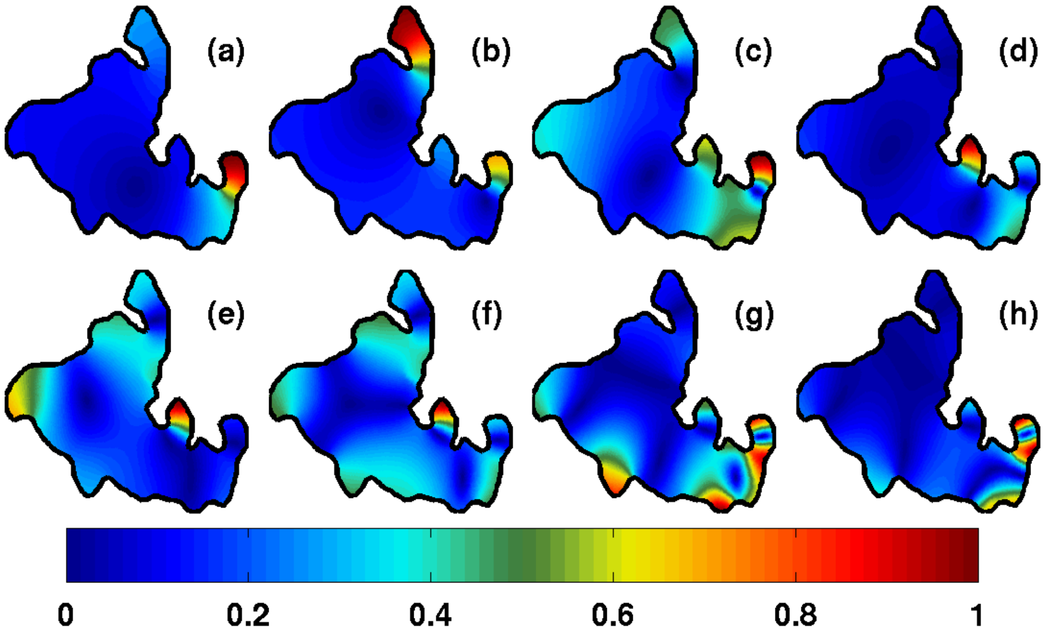

Figure 6.16: Like Figure 6.15, but the amplitudes $A(x, y)$ are plotted. $A(x, y)$ is scaled to have a maximum value of 1.

duces a corresponding family of rotational waves into the spectrum. These rotational modes are analogous to planetary-scale Rossby waves that exist due to the meridional gradient of the Coriolis parameter. The application of the method to Lake Pinehurst that features both irregular geometry and variable bottom bathymetry yielded modes that in general consisted of small (localized) cells that exhibit their own local rotation and propagation properties. The structure of the modes gave further insight into how wave phenomena would be amplified both in confined narrow bays of lakes and also in shallow regions, as discussed previously.